



UNIVERSITY OF LEEDS

This is a repository copy of *Effect of cooling rate and chromium doping on the microstructure of Al-25 at.% Ni Raney type alloy*.

White Rose Research Online URL for this paper:
<http://eprints.whiterose.ac.uk/128314/>

Version: Accepted Version

Article:

Hussain, N, Mullis, AM and Forrester, JS (2018) Effect of cooling rate and chromium doping on the microstructure of Al-25 at.% Ni Raney type alloy. *Journal of Alloys and Compounds*, 744. pp. 801-808. ISSN 0925-8388

<https://doi.org/10.1016/j.jallcom.2018.02.123>

© 2018 Elsevier B.V. This manuscript version is made available under the CC-BY-NC-ND 4.0 license <http://creativecommons.org/licenses/by-nc-nd/4.0/>

Reuse

This article is distributed under the terms of the Creative Commons Attribution-NonCommercial-NoDerivs (CC BY-NC-ND) licence. This licence only allows you to download this work and share it with others as long as you credit the authors, but you can't change the article in any way or use it commercially. More information and the full terms of the licence here: <https://creativecommons.org/licenses/>

Takedown

If you consider content in White Rose Research Online to be in breach of UK law, please notify us by emailing eprints@whiterose.ac.uk including the URL of the record and the reason for the withdrawal request.



eprints@whiterose.ac.uk
<https://eprints.whiterose.ac.uk/>

Effect of Cooling Rate and Chromium Doping on the Microstructure of Al-25 at.% Ni Raney Type Alloy

Naveed Hussain^a, Andrew M Mullis^a, Jennifer S Forrester^a

^aSchool of Chemical & Process Engineering, University of Leeds, Leeds LS2 9JT, UK.

Abstract

Al-25 at.% Ni and Al-23.5 at.% Ni-1.5 at.% Cr alloys were synthesised via gas atomization to study the effect of rapid cooling on the microstructure and phase composition of Raney type catalyst precursor powders. In the undoped powders, the three phases, Al₃Ni₂, Al₃Ni, and Al-Al₃Ni eutectic were identified, while in the Cr-doped powders the additional phase Al₁₃Cr₂ was also identified. Extensive substitution of Ni onto the Cr lattice sites is observed, which generates the observed phase fraction of Al₁₃Cr₂. Elemental mapping and quantitative image analysis of backscattered electron micrographs indicates that the Al₁₃Cr₂ phase precipitates late in solidification, probably direct from the melt, during the final stages of Al₃Ni growth. As such, this explains previous observations that Cr is found on the surface of the activated catalyst without the need to invoke migration of Cr. Leaching of such an Al-rich compound offers a plausible explanation for the enhanced catalytic activity observed in Cr-doped Raney catalysts.

Keywords

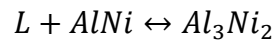
Intermetallics; Rapid-solidification; Microstructure; Catalysis; Metals and alloys

1.0 Introduction

Skeletal metal catalysts, such as Raney Ni, are a popular choice of catalyst for hydrogenation reactions. The traditional Raney Ni alloy, discovered by Murray Raney, comprises a 50-50 wt% mixture of Ni and Al, although due to the lower atomic mass of Al compared to Ni, this is

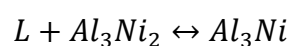
approximately 68.5 at.% Al. The production of Raney Ni catalysts is traditionally performed by castings the alloy into ingots, which are then crushed into a coarse powder to allow activation by leaching.

It has been determined that the precursor Al-Ni alloy contains 3 phases, irrespective of the initial alloy composition; Al_3Ni_2 (Space group: $P\bar{3}m1$ [1]), Al_3Ni (Space Group: $Pnma$ [1]) and an Al- Al_3Ni eutectic [2]. With reference to the Al-Ni phase diagram, the first phase to appear from the Ni-68.5 at.% Al melt will be AlNi when cooling to 1623 K (see fig.1). At approximately 1406 K the AlNi will react with the remaining liquid via the peritectic reaction:



to give Al_3Ni_2 . It has been shown that during the slow cooling appropriate to producing large ingots, and also at higher cooling rates such as during gas atomisation, the final microstructure of the Ni-68.5 at.% Al alloy rarely contains AlNi. This has led to some debate as to whether the AlNi phase is bypassed as the primary solidification phase in favour of direct solidification of Ni_2Al_3 from the melt, or whether the peritectic reaction at 1406 K is sufficiently rapid so as to go to completion [2]. However, this question has been resolved using X-ray diffraction (XRD) experiments conducted by Lengsdorf et al. Using in-situ time-resolved XRD during solidification on levitated drops at the ESRF synchrotron radiation facility, the diffraction pattern of AlNi was detected, thereby establishing that for the Ni-68.5 at. % Al composition, Al_3Ni_2 must form via the peritectic, not direct from the melt [3].

At 1127 K the Al_3Ni_2 undergoes a second peritectic reaction to form Al_3Ni :



As with many peritectic reactions, this is observed to form a shell of the secondary phase (Al_3Ni) surrounding the core of the remaining unreacted primary phase (Al_3Ni_2). The contrast between the two peritectic reactions at 1406 K and 1127 K is that the former is a rapid reaction, therefore allowing the $\text{AlNi} \rightarrow \text{Al}_3\text{Ni}_2$ reaction to go to completion. Conversely, the latter peritectic reaction at 1127 K is much slower, allowing some of the Al_3Ni_2 to be retained. The reason for this contrast may be due to the similarity between the structures of AlNi and Al_3Ni_2 ; Al_3Ni_2 is a trigonal extension of the cubic B2 AlNi phase in which every third plane of Ni atoms perpendicular to the trigonal axis is missing [4]. On the other hand, since Al_3Ni is a stoichiometric intermetallic, the rate of solid-state diffusion through the growing shell of Al_3Ni will be sluggish, as it is difficult for the line compound to support a concentration gradient to drive diffusion. This places the $\text{Al}_3\text{Ni}_2 \rightarrow \text{Al}_3\text{Ni}$ peritectic in Type C of the classification described by Kerr & Kurz [5]. This classification is characterised by slow transformation rates during the solid-solid peritectic transformation (SSPT) stage of the reaction.

The final stage of solidification occurs at 913 K, wherein the residual liquid solidifies to an Al- Al_3Ni eutectic [6]:



During the preparation of the catalyst, the precursor alloy is leached in concentrated sodium hydroxide solution, removing the Al from both the eutectic and the intermetallic phases, leaving nano-crystalline Ni, whilst also producing a suitable atmosphere to activate the Nickel catalyst. After the leaching process, aqueous washing is used to remove the dissolved aluminate and excess alkali [7]. The remaining catalyst, which is highly pyrophoric, can then be stored in water or alcohol [6].

Depending upon the preparation of the precursor alloy, it is observed that there is a variation between the amounts of each phase present, even if the composition remains the same. Cooling rate in

particular has been shown to affect the phase composition of the precursor alloy, with higher cooling rates tending to suppress the $\text{Al}_3\text{Ni}_2 \rightarrow \text{Al}_3\text{Ni}$ peritectic, leading to greater retained Ni_2Al_3 with consequently less Al_3Ni . The phase composition of the precursor has an important effect on the properties of the activated catalyst. It has been found that Al_3Ni is the least resistant phase to leach, resulting a highly active catalyst but with poor mechanical strength [2]. Consequently, catalysts based on precursor alloys with high Al_3Ni concentrations are not suitable for applications such as slurry and tubular bed reactors [8]. Al_3Ni_2 is more resistant to leaching, but when leached successfully can maintain greater structural integrity than an Al_3Ni based catalyst, due mainly to incomplete leaching. In a commercial catalyst produced by cast-crush processing of slowly cooled ingots, it is common that there is more Al_3Ni_2 in the microstructure than Al_3Ni . Around 58 wt.% of Al_3Ni_2 is expected from the commercial alloy using regular cooling rate [9], with the remaining 42 wt.% made up of Al_3Ni . Very small amounts of Al eutectic may be present (<1 wt.%) [9].

Rapid solidification has been investigated as a route to producing improved Raney type catalysts, both because the higher cooling rates alter the distribution of phases, and because it provides a route to the utilisation of more Al-rich compositions [9] [10]. The performance of gas atomised Raney powders has been investigated extensively as part of the IMPRESS project, with cooling rates between $200 - 5000 \text{ K s}^{-1}$ for typical gas atomised powders in the size range $38\text{-}212 \mu\text{m}$ [11]. It was found that for the hydrogenation of nitrobenzene, relative to a bench mark activity for cast-crush 50-50 wt% catalyst of $3.5 \text{ mol kg}^{-1} \text{ min}^{-1}$, the gas atomised powder ($106\text{-}150 \mu\text{m}$ size fraction) showed an activity of only $1.4 \text{ mol kg}^{-1} \text{ min}^{-1}$ for the 50-50 wt% composition, though this could be increased to $4.8 \text{ mol kg}^{-1} \text{ min}^{-1}$ for a 75 at.% Al catalyst ($106\text{-}150 \mu\text{m}$ size fraction) [12].

Similar conclusions have been drawn from theoretical studies, such as that conducted by Tourret et al. Simulations were performed using the public binary database PBIN within the ThermoCalc

software[†] [13]. The alloy thermo-physical properties used were the same as a previous solidification model for the solidification of electromagnetically levitated Al-25 at.% Ni droplets [14]. Particle sizes of 10 μm , 60 μm and 120 μm diameter were modelled, wherein solidification times ranged from 1.3×10^{-3} s (10 μm) to 0.2 s (120 μm). It was found that in an Ni-80 at.% Al alloy, the increase in particle size resulted in an increase in the Al_3Ni phase fraction and a decrease in the Al_3Ni_2 phase fraction at all particle sizes. When more Al was introduced to the initial alloy composition, this was only observed in larger particles.

The activity of Raney Ni catalysts can be improved by introducing a 3rd metal, known as a promoter, or dopant. The most common promoters used with Raney Ni are Cr, Fe and Mo, but research has been conducted on other promoters such as Cu, La, Co and Ti. During the preparation of the alloy, the promoter can be added to the melt, usually in small quantities (1-3%) depending on the reaction to be catalysed [6]. One study found that all of the aforementioned promoters increase the activity of the catalyst, but that Molybdenum was found to be the most effective for the hydrogenation of butyronitrile and acetone [15].

Research has been carried out on the influence of Chromium as a promoter in Raney Ni catalysts. It has been found that the optimum level of Chromium required in the Raney Ni alloy is 1.5 wt% for the hydrogenation of butyronitrile, acetone and sodium p-nitrophenolate [6]. Bonnier et al. [16] studied the activity of Cr-doped Raney Ni, prepared by mechanically mixing Al-Ni and Cr-Al alloys, on the hydrogenation of acetophenone. It was found that there was indeed an increase in activity, with the Chromium being strongly segregated to the surface in an oxidised state. It was further found that due to the presence of chromium oxide, the residual aluminium, in a metallic state, is retained more than that of an undoped AlNi alloy. Metallic aluminium seems to inhibit reactions such as the hydrogenation of carbonyl groups [17] which are promoted by the chromium oxide [6]. Work by

[†] <http://www.thermocalc.se>.

Pisarek et al. also found that surface segregated Cr promoted catalytic activity for the hydrogenation of isophorone to dihydroisophorone, but also that Cr deactivates the Ni–Al catalyst for the reaction of dihydroisophorone hydrogenation [18]. In previous work it has been assumed, due to the chemical similarity between Ni and Cr, that Cr substitutes randomly for Ni [16].

The IMPRESS project, as well as looking at the effect of high cooling rate on the activity of Raney Ni catalysts, also investigated the effect of dopants upon activity. It was found that, by the addition of 1.5 at.% Cr to a 75 at.% Al alloy, the catalytic activity for the hydrogenation of nitrobenzene was increased from $4.8 \text{ mol kg}^{-1} \text{ min}^{-1}$ to $11.6 \text{ mol kg}^{-1} \text{ min}^{-1}$ (both 106-150 μm size fraction). This is comparable to the effect of adding 1.5 at.% Cr to a standard 50-50 wt.% cast-crush catalyst, wherein the catalytic activity increases from $3.5 \text{ mol kg}^{-1} \text{ min}^{-1}$ to $7.35 \text{ mol kg}^{-1} \text{ min}^{-1}$. However, the underlying mechanism for this astonishing 140% increase in catalytic activity of the doped, gas atomised powders, was never established. In this paper, we reanalyse the original gas atomised precursor alloy powders in order to elucidate the mechanism for this increased catalytic activity.

2.0 Experimental procedure

Powders were produced via the close coupled gas atomisation technique. Material was produced in 6 kg batches, with each batch composition 25% Ni + 75% Al or 23.5% Ni + 75% Al + 1.5% Cr respectively (all are given in at.%). In each case, the melt pour temperature was 1813 K, a superheat of $\approx 190 \text{ K}$ above the liquidus temperature. Atomisation takes place at the tip of a boron nitride nozzle, 5 mm in diameter, which is fed by liquid metal at a pressure of 4 kPa through a 2 mm central bore. The molten metal is stripped off the circumferential edge of the nozzle by 18 high pressure (3.5 MPa) argon gas jets, wherein it solidifies in-flight, producing a fine, highly spherical powder. The typical gas velocity is estimated at Mach 3 and the gas and melt flow rates were $48.65 \times 10^{-3} \text{ kg s}^{-1}$ and $15.75 \times 10^{-3} \text{ kg s}^{-1}$ respectively. Full details of the experimental procedure are given [11]. The solidified particulate samples were then sieved into standard sieve size, with the

following size fractions being selected for study: $53\mu\text{m} < 75\mu\text{m}$, $75\mu\text{m} < 106\mu\text{m}$ and $150\mu\text{m} < 212\mu\text{m}$. Cooling rates vary due to particle size, with estimated mean cooling rates for these size fractions being 320, 1000 and 1800 K s^{-1} respectively [11].

XRD was carried out on the AlNi and AlNiCr samples using a Bruker D8 diffractometer with $\text{Cu-K}\alpha$ radiation, collimated through a 1 mm-wide rectangular opening. Samples were mounted as a flat layer of powder within a low-background silicon sample holder. Each sample was subjected to a 4-hour and a 16 hour scan to assess the influence of scan duration upon noise in each of the resulting diffraction pattern. The XRD patterns were analysed using the HighScore program, where the peaks were compared to the International Centre for Diffraction Data (ICDD) database to determine the phases present. Rietveld refinement was carried out using the General Structure Analysis Software (GSAS) program [19] with the EXPGUI [20] interface.

The Rietveld refinement was used to determine several crystallographic features of interest in the as-solidified AlNi and AlNiCr alloys. These included determining the phases present, the phase proportions, and the elemental occupancies with each of the phases. The undoped and Cr doped sample XRD patterns were refined and acceptable fits were achieved, leading to consistent results in the phase fractions. The parameters varied including 2Θ zero, scale factor, preferred orientation and background in a shifted Chebyshev model.

There was an added complication in the Cr-doped sample XRD patterns. The unit cell of $\text{Al}_{13}\text{Cr}_2$ is very large, and as such includes a large number of atomic positions (see Figure 3). In performing a sensitivity analysis of the response of the fit to these parameters it was found that, if a strict ‘best-fit’ was sought, the resulting phase fractions were sensitive to small changes in the fitting parameters. Conversely, if we allowed the quality of the fit to be relaxed somewhat, R_p between 1.36% and 1.72%, phase fractions were obtained which showed much less sensitivity to the fitting parameters.

In comparison, the undoped samples achieved R_p between 0.72% and 0.99%, which indicates a better fit. This latter approach has been adopted in the results presented in Section 3.2.

Samples were prepared for scanning electron microscopy (SEM) analysis by mounting in TransOptic™ resin using a Buehler SimpliMet™ 3000 Automatic Mounting Press with a pressure of 180 bar. The heating and cooling times were 3 mins and 12 mins, respectively. Samples were then ground using the MetaServe™ 250 grinder-polisher machine from Buehler, before polishing using 3 TexMet C polishing cloths each using 6 μm , 3 μm and 1 μm diamond paste, respectively. Samples were then cut using the Buehler Accutom 50 to less than 10 mm in height and fixed to an SEM stub for analysis using a Hitachi SU8230 scanning electron microscope. The samples were sputter coated with a layer of carbon in order to minimise charging.

SEM in backscattered detection mode was used and appropriate magnification was selected for each sample on the Hitachi SU8230 microscope. The high-resolution settings were 5 kV accelerating voltage (V_{acc}) and 20 μA probe current (I_e). For samples between 150 μm < 212 μm in diameter, the magnification was approximately 3000x and samples of 53 μm < 75 μm diameter this was increased to approximately 5000x magnification. During Electron Dispersive X-Ray Spectroscopy (EDX) the spot size was set to 450 nm and the frame speed set to approximately 2 mins due to the limited amount of Cr within the sample. The low Cr content meant that a relatively slow scan was required in order to reduce noise in the scan. 20 frames were taken per sample during mapping of the Cr localisation, resulting in a 40-minute scan per sample.

3.0 Results

3.1 CALPHAD Modelling

A Scheil solidification sequence was calculated for $\text{Al}_{75}\text{Ni}_{(25-x)}\text{Cr}_x$ using the CALPHAD modelling software package MTDATA [21] with version 4.3 of the SGTE database. The equilibrium solidification pathway for $x = 1.5$ was determined as:

1353 K: $\text{L} \rightarrow \text{Al}_3\text{Ni}_2$ (primary)

1139 K: $\text{L} \rightarrow \text{Al}_3\text{Ni}_2 + \text{Al}_4\text{Cr}$ (primary)

1117 K: $\text{L} + \text{Al}_3\text{Ni}_2 \rightarrow \text{Al}_3\text{Ni} + \text{Al}_4\text{Cr}$ (peritectic)

1069 K: $\text{L} + \text{Al}_4\text{Cr} \rightarrow \text{Al}_3\text{Ni} + \text{Al}_{11}\text{Cr}_2$ (peritectic)

983 K: $\text{L} + \text{Al}_{11}\text{Cr}_2 \rightarrow \text{Al}_3\text{Ni} + \text{Al}_{13}\text{Cr}_2$ (peritectic)

915 K: $\text{L} \rightarrow \text{Al}_3\text{Ni} + \text{Ni}$ (eutectic)

From the Scheil solidification sequence, three additional compounds were identified as potentially present. The first is Al_4Cr , which is predicted to form via primary solidification direct from the melt. If present, Al_4Cr may be located near the centre of grains. Its formation at 1139 K may therefore also interfere with the $\text{L} + \text{Al}_3\text{Ni}_2 \rightarrow \text{Al}_3\text{Ni}$ peritectic reaction at 1117 K, as extensive deposition of this phase might be expected to isolate the Al_3Ni_2 phase from the liquid. The second additional compound is $\text{Al}_{11}\text{Cr}_2$, which is predicted to form via a peritectic reaction between the Al_4Cr phase and the remaining liquid. If formed via this route, any $\text{Al}_{11}\text{Cr}_2$ present is expected to be located interspersed with the Al_3Ni phase. The third additional compound identified is $\text{Al}_{13}\text{Cr}_2$, formed via the final peritectic reaction between $\text{Al}_{11}\text{Cr}_2$ and the residual melt at 1069 K. The Scheil solidification sequence has initially been used to guide the analysis of XRD data by suggesting which additional phases may be present in the Cr-doped material, although subsequent identification of the location of phases within the microstructure is expected to provide information relating to which reactions were active during solidification.

3.2 XRD Measurements

Analysis of the XRD patterns showed that the 3 predicted Al-Ni phases, Al_3Ni_2 , Al_3Ni and Al (in the Al- Al_3Ni eutectic), exist in both the undoped and doped AlNi alloys, regardless of the particle size fraction. Example patterns for the undoped and Cr-doped alloys are given in Figures 2 and 3 respectively, in both cases for the 150-212 μm sieve fraction. The XRD pattern for the Cr-doped sample shows additional peaks. A preliminary analysis, performed using the HighScore software[‡], suggests that these peaks may tentatively be associated with the $\text{Al}_{13}\text{Cr}_2$ phase.

Information can be also obtained from the XRD scans in Figures 2 and 3 to determine the effect of droplet size upon phase composition, using Rietveld refinement. Examples of the Rietveld fits to the raw XRD data, and the residuals between the calculated and experimental data are also shown in Figures 2 and 3.

Processing of the Rietveld refinement was difficult with respect to the $\text{Al}_{13}\text{Cr}_2$ phase. This phase is variously referred to in the literature not only as $\text{Al}_{13}\text{Cr}_2$, but also Al_7Cr and $\text{Al}_{45}\text{Cr}_7$. However, all three are documented as belonging to the same space group (space group: C2/m [22]). The similarities in the crystal structures indicate that these are alternate designations for the same phase. Irrespective of the designation, there is very little information for this phase in the literature. ICDD data is absent above 45° deg (2Θ) for $\text{Al}_{13}\text{Cr}_2$ and 60° deg (2Θ) $\text{Al}_{45}\text{Cr}_7$, with significant differences between the $\text{Al}_{13}\text{Cr}_2$ and $\text{Al}_{45}\text{Cr}_7$ reference patterns (00-029-0014 and 04-004-3588 respectively), even in the region of overlap. Moreover, no data was found for Al_7Cr . As a consequence, in a number of previous studies the $\text{Al}_{13}\text{Cr}_2$ phase has been omitted from the refinement due to the lack of crystal structure data (see e.g. [23]). To obtain a fit, a model of the $\text{Al}_{13}\text{Cr}_2$ unit cell had to be constructed based on published atom coordinates [22].

[‡] <http://www.panalytical.com>.

The crystal structure data for the $\text{Al}_{13}\text{Cr}_2$ phase generates a large number of lattice planes, which in turn generates a very dense array of hkl markers (the dark brown markers in Figure 3). Also apparent in Figure 3 is a departure of the baseline from linear around 45° deg. This is likely to be the result of the combination of a dense number of planes generated by the combination of all of the phases present within that region of the XRD pattern. In any case, the fitting of these patterns had to be done carefully, in order to produce reliable results.

The additional peaks observed in all size fractions of Cr-doped AlNi were identified as a single monoclinic $\text{Al}_{13}\text{Cr}_2$ phase (space group: $C2/m$ [22]) and consistent, stable phase fraction data was obtained. No evidence of either Al_4Cr or $\text{Al}_{11}\text{Cr}_2$ was found. Consequently, if the solidification sequence was as predicted by the Scheil calculations, this would suggest that both Al-Cr peritectic reactions were able to go to completion.

Weight fractions obtained from the Rietveld refinements are presented in Tables 1 and 2. With increasing particle size, there is more Al_3Ni and less Al_3Ni_2 . The amount of Al eutectic also decreases as the particle size increases. This agrees with the expectation that the higher cooling rates experienced by the smaller droplets allow less time for the peritectic conversion of Al_3Ni_2 to Al_3Ni to proceed. This in turn results in a more Al-rich residual liquid, increasing the volume fraction of eutectic.

The effect of Cr doping is shown in Table 2. The phase fractions with regard to the non-Cr-bearing phases follow a similar trend in relation to the size fractions, and therefore cooling rate, as for the undoped AlNi particles. However, it is also clear that there are significant amounts of $\text{Al}_{13}\text{Cr}_2$ present, which is unexpected given the low level of Cr doping in the alloy. Based on a mass balance calculation, the maximum weight fraction of $\text{Al}_{13}\text{Cr}_2$ without substitution of Ni for Cr is approximately 9.5 wt%. The weight fractions of $\text{Al}_{13}\text{Cr}_2$ in Table 2 exceed the maximum weight fraction possible (without substitution). It is therefore suggested that Ni substitutes into the Cr lattice

within the $\text{Al}_{13}\text{Cr}_2$ phase. A similar conclusion was drawn in [8], in which it was found that a Ti-doped Raney type alloy contained a $(\text{Ti,Ni})\text{Al}_3$ phase with the $I4/mmm$ TiAl_3 crystal structure. The 4th phase should therefore be more correctly designated as $\text{Al}_{13}(\text{Cr,Ni})_2$, although we continue to refer to the phase as $\text{Al}_{13}\text{Cr}_2$, with the understanding that Ni substitution for Cr is implied. The fractional coordinates of Cr in the $\text{Al}_{13}\text{Cr}_2$ phase include 3 sites with a multiplicity of 2, 4 and 8 respectively. When conducting Rietveld refinement, it was found that there was a deficiency of Cr on all 3 sites, with the lowest deficiency being 0.25 in the first site, with the highest Cr deficiency being more than 0.8 in the 3rd site, representing a total Cr deficiency of more than 40% across the Cr atomic sites. Rietveld refinement was also conducted with the assumption that Ni substitutes into the Cr lattice, and all the Cr deficiencies within the $\text{Al}_{13}\text{Cr}_2$ were accounted for by Ni. Further analysis of the $\text{Al}_{13}\text{Cr}_2$ phase containing Ni can be found in section 3.3.

Table 1

Weight fractions of each phase in Al-25 at.% Ni obtained using Rietveld refinement of XRD data.

	Size fraction	Weight %			
		Al_3Ni_2	Al_3Ni	Al eutectic	$\text{Al}_{13}\text{Cr}_2$
Al-25 at.% Ni	150 μm < 212 μm	33.5	53.8	12.7	N/A
	75 μm < 106 μm	34.1	50.4	15.5	N/A
	53 μm < 75 μm	36.3	47.3	16.4	N/A

Table 2

Weight fractions of each phase in Al-23.5 at.% Ni-1.5 at.% Cr obtained using Rietveld refinement of XRD data.

	Size fraction	Weight %			
		Al ₃ Ni ₂	Al ₃ Ni	Al eutectic	Al ₁₃ Cr ₂
Al-23.5 at.% Ni	150μm < 212μm	29.1	45.2	9	16.8
-1.5 at. %Cr	75μm < 106μm	30.4	38.9	13.7	16.9
	53μm < 75μm	32.9	37.1	13.4	16.6

3.3 SEM Microstructure characterisation

Figures 4 a and b show SEM micrographs of the largest and smallest size fractions of the undoped Raney powders. The three phases are clearly distinguishable in backscatter mode with Al₃Ni₂ appearing lightest (highest mean atomic number) and the Al-Al₃Ni eutectic darkest (lowest mean atomic number), with Al₃Ni appearing mid-grey. The characteristic core-shell morphology typical of peritectic reactions is visible, with many of the Al₃Ni₂ dendrites displaying a surface shell of Al₃Ni. There is a noticeable difference in the microstructures with decreasing particle size; the microstructures of the smaller droplets appear more dendritic in character. In contrast, the larger droplets have a microstructure that appears more globular. Figure 5 shows a similar SEM micrograph as figure 4a but with a higher magnification in order to expose the Al-Al₃Ni eutectic, this is observed in all samples including Cr doped samples. The morphology observed is typical of a rod-like eutectic which is expected as one of the phases (Al₃Ni) has a low volume fraction compared to the other. In the SEM backscattered electron images in Figures 6a and 6b, the Cr doped AlNi alloys display the

same microstructural characteristics as the undoped alloys. Again, the Al_3Ni_2 can be seen at the core of the dendrites encased in a shell of darker material. One difference in the microstructure of the doped alloys is how defined the dendrites are; in each particle size fraction, the dendrites appear more defined than the corresponding undoped particles. The dendrites become more defined with reducing particle size.

Figure 7 shows a backscattered micrograph for the 150-212 μm sieve fraction of the Cr doped alloy, overlaid with an EDX map for Cr to identify regions of Cr localisation. The majority of the Cr present within the sample is co-located with the Al_3Ni phase, largely on the boundary between Al_3Ni and the Al eutectic, with lesser amounts present in what appears to be the Al eutectic. This is not in accordance to the Scheil calculation, which suggests that $\text{Al}_{13}\text{Cr}_2$ develops from a series of peritectic reactions, the precursor for which is Al_4Cr which is expected to be co-located within the Al_3Ni_2 phase. Based upon its location within the microstructure, we hypothesise that $\text{Al}_{13}\text{Cr}_2$ forms directly from the liquid as a primary solidification phase, probably towards the end of Al_3Ni growth.

Given that the Cr-doped alloy contains 4 phases, with significant amounts of the $\text{Al}_{13}\text{Cr}_2$ phase present, we reason that this should be evident within the microstructure. In backscattered imaging, $\text{Al}_{13}\text{Cr}_2$ should appear darker than Al_3Ni , due to the lower mean atomic number, but not as dark as the Al- Al_3Ni eutectic.

Figures 8 a and b show histograms of the grey-level intensities for the SEM micrographs of the Cr-doped alloys in the 150-212 μm and 53-75 μm size fractions respectively. Three distinct peaks are visible, corresponding to the presence of a particular phase; the darkest is the Al-rich eutectic with the lightest corresponding to Al_3Ni_2 . It is worth noting that the smallest peaks in each histogram on the far right are due to pull-out in the microstructure. Pull-out occurs when the Al-eutectic becomes loose from the mounted, ground and polished sample. In addition to the three distinct peaks, each histogram contains a less well developed 4th peak, which in Figure 8b is evident as a shoulder to the

right of the Al_3Ni peak. This peak is in the correct position to correspond to $\text{Al}_{13}\text{Cr}_2$ phase, so we now investigate the spatial distribution of material within the microstructure corresponding to this peak.

The peak corresponding to $\text{Al}_{13}\text{Cr}_2$ in Figure 8a has a maximum at 99 and is delimited by grey levels of 83 and 101 at the dark and light ends of the spectrum respectively. The grey level range 83-101 within the micrograph is shown highlighted in Figure 9 and corresponds closely with the expected location of the $\text{Al}_{13}\text{Cr}_2$ phase, i.e. co-located with the Al_3Ni phase at the Al_3Ni -eutectic interface. This is confirmed in Figure 10 in which we overlay the grey level map with the EDX Cr-map from Figure 7, wherein an almost exact correspondence between the grey level and Cr localisation may be observed. This provides a high level of confidence in associating this grey level range with the $\text{Al}_{13}\text{Cr}_2$ phase.

The grey level range 83-101 in Figure 9 represents 21% of the total pixel count, hence an estimate of 21 vol.% of $\text{Al}_{13}\text{Cr}_2$ in the sample. For comparison, converting the data in Table 2 to volume %, 16.8 wt.% $\text{Al}_{13}\text{Cr}_2$ is 20.1 vol.%. For the other two size fractions; in the 75-106 μm size range the $\text{Al}_{13}\text{Cr}_2$ peak covers the grey range 76-96, which is 18.5% of the total pixel count, while for the 53-75 μm size range the $\text{Al}_{13}\text{Cr}_2$ peak covers the grey range 72-92, which is 19.1% of the total pixel count. The corresponding weight fractions from the Rietveld analysis are 16.9 and 16.6 wt.%, which convert to 19.6 and 19.4 vol.% respectively. We consider these to be in excellent agreement and to serve as confirmation of the Rietveld analysis of the XRD data.

Point EDX analysis was conducted on the $\text{Al}_{13}\text{Cr}_2$ phase of the Cr doped samples to determine the composition of this phase. Ni was expected to substitute for the Cr due to the high amounts of $\text{Al}_{13}\text{Cr}_2$ in the final alloys. Table 3 shows the elemental composition of $\text{Al}_{13}\text{Cr}_2$ for each sample size fraction. Four spots from each size fraction were chosen in the $\text{Al}_{13}\text{Cr}_2$ phase with the average atomic % and standard error shown in Table 3. The amount of Cr found in the $\text{Al}_{13}\text{Cr}_2$ phase is in agreement

with the total amount of Cr added to the alloy, on the assumption that all of the Cr is located within the $\text{Al}_{13}\text{Cr}_2$ phase. However, it is also noticeable that in all of the samples the $\text{Al}_{13}\text{Cr}_2$ appears to be Al-deficient (at stoichiometry we would expect 86.6 at.% Al) and consequently rich in Cr + Ni. This could be that Ni is substituting not only for Cr but also for Al, although the result could also be an artefact of the EDX process, which has a relatively large interaction volume compared to the size of the phases present. The large interaction volume could mean that Ni is identified in the $\text{Al}_{13}\text{Cr}_2$ phase but is actually located in the Al_3Ni phase surrounding or below the phase being analysed.

Table 3

The elemental composition of $\text{Al}_{13}\text{Cr}_2$ for each sample size fraction of Al-23.5 at.% Ni-1.5 at.% Cr obtained using Point EDX analysis.

Spectrum	Atomic % (Standard error)		
	N=2	N=1	N=4
	150 μm < 212 μm	75 μm < 106 μm	53 μm < 75 μm
Al	76.92 (3.19)	74.28 (9.17)	82.8 (7.43)
Cr	8.31 (5.83)	6.55 (2.92)	6.65 (2.39)
Ni	14.78 (5.83)	19.18 (10.65)	10.56 (5.33)

4.0 Discussion

It is clear from the above results that particle size and doping with a third element can have a significant effect on both the microstructure and phase composition of Raney type precursor alloys. An obvious change with respect to particle size is that, as the size decreases the fraction of Ni_2Al_3

present increases while that of Al_3Ni decreases. This may be explained due to the dissimilar cooling rates of different sized particles, with the larger particle requiring longer cooling time and therefore allowing more time for the sluggish peritectic reaction to convert Ni_2Al_3 into Al_3Ni . However, cooling rate also appears to mediate microstructural changes, with the large particles displaying a more globular microstructure than the smaller particles, which appear fully dendritic. Large particles may be subject to more stirring due to the larger shear force acting upon the particle surface from the supersonic gas. Smaller particles may not be subject to the same level of shear force since they are more easily carried along with the high velocity gas stream. Moreover, the lower cooling rates, and hence longer solidification times, applicable to the large particles mean that there is a longer time for the shear to act to disrupt the microstructure. In addition, higher cooling rates in the smaller particles, coupled with the melt sub-division effect, will lead to higher undercooling than the larger particles, with this undercooling contributing to the more dendritic character of the microstructure in the smaller particles.

An interesting and unexpected outcome of Cr-doping is that even the larger droplets are observed to form a fully dendritic microstructure, with little evidence of the globular structures observed in the undoped alloys. The shear forces, cooling rates and solidification times are expected to be comparable between the doped and undoped alloys of the same particle size. Consequently, any difference in microstructure must be due to changes in the solidification dynamics mediated by the addition of Cr. As the EDX results indicate, virtually no Cr is co-located with the Ni_2Al_3 phase, meaning almost total rejection of Cr from the growing solid during this initial phase of solidification may be postulated. We conjecture that it is this additional solute flux, and the consequent need to diffuse Cr away from the growing solid, that leads to this increased dendritic character in the microstructure.

The most significant effect of Cr-doping is the formation of an extensive 4th phase, $\text{Al}_{13}\text{Cr}_2$. The identification of this phase in the Cr-doped samples, together with the EDX results, indicate that

virtually all of the Cr added to the alloy is present within this phase. This conclusively refutes the assertion that Cr randomly substitutes for Ni [16]. However, the spatial location of the $\text{Al}_{13}\text{Cr}_2$ within the microstructure is not consistent with the CALPHAD generated Scheil solidification sequence, which would expect Al_4Cr to be the second phase to form, after Ni_2Al_3 . Instead, the Cr appears to be retained within the liquid during the early phase of solidification, with all of the Cr contained within the $\text{Al}_{13}\text{Cr}_2$ phase.

The most likely explanation for this is that Al_4Cr does not nucleate easily under the conditions prevailing in the gas atomised powders. Li et al. [24] describe $\epsilon\text{-Al}_4\text{Cr}$ as being a complex phase belonging to the Cmcm orthorhombic space group with a unit cell containing 55 atoms, 40 of which have icosahedral ordering. As such $\epsilon\text{-Al}_4\text{Cr}$ has been extensively studied as a potential quasicrystal [25], although the nucleation of such a phase could be easily suppressed. Similarly, $\eta\text{-Al}_{11}\text{Cr}_2$, the next phase predicted to form in the equilibrium Scheil solidification sequence, also displays complex icosahedral ordering (C2/c space group, 80 atoms per unit cell) [26], wherein nucleation of this phase may also be difficult. Performing the Scheil calculation again with these two phases suppressed we would predict seeing the direct solidification of $\text{Al}_{13}\text{Cr}_2$ from the melt, albeit at a somewhat higher temperature (1100 K) than predicted for its formation via the peritectic decomposition of $\text{Al}_{11}\text{Cr}_2$ (983 K). Such a solidification sequence would place the formation of the $\text{Al}_{13}\text{Cr}_2$ phase coincident with Al_3Ni growth, in good agreement with the experimental data obtained in this study.

The proposed solidification sequence provides a framework in which the dramatic increase in catalytic activity mediated by the addition of 1.5 at.% Cr (140% increase in activity for the hydrogenation of nitrobenzene) can be explained. Leaching the Cr doped powders from this study would give Cr on the surface of the activated catalyst without the need for migration of Cr. After the Al eutectic is removed, the first phase that would be encountered is $\text{Al}_{13}\text{Cr}_2$ which, when leached, would give a surface Cr coating as observed by Bonnier et al. [16]. Moreover, as $\text{Al}_{13}\text{Cr}_2$ is significantly more Al-rich than Al_3Ni , upon leaching it would be expected to give a more open nano-

porous structure. This alone would be expected to increase catalytic activity, even without any consideration of whether Cr is a more active catalytic species than Ni. This finding therefore also point the way to potential future developments in Raney type alloys, as any Al-rich (> 85 at.%) phase precipitating late in solidification is likely to result in enhanced catalytic activity.

Acknowledgements

This work was supported by the Engineering and Physical Sciences Research Council Doctoral Training Partnership [ref. 1633900]

References

- [1] M. Ellner, U. Kattner and B. Predel, "Constitutional and structural investigations in the aluminum-rich part of the Ni-Al and Pt-Al systems," *Journal of the Less Common Metals*, vol. 87, no. 2, p. 305, 1982.
- [2] F. Devred, A. H. Gieske, N. Adkins, U. Dahlborg, C. M. Bao, M. Calvo-Dahlborg, J. W. Bakker and B. E. Nieuwenhuys, "Influence of phase composition and particle size of atomised Ni–Al alloy samples on the catalytic performance of Raney-type nickel catalysts," *Applied Catalysis A: General*, vol. 356, pp. 154-161, 2009.
- [3] R. Lengsdorf, D. Holland-Moritz and D. M. Herlach, "Anomalous dendrite growth in undercooled melts of Al-Ni alloys in relation to results obtained in reduced gravity," *Acta Materialia*, vol. 62, pp. 365-367, 2009.
- [4] A. Taylor and N. J. Doyle, "Further Studies on the Nickel-Aluminum System. I. The [I-NiAl and 6-Ni2Al3 Phase Fields," *Journal of Applied Crystallography*, vol. 5, no. 3, pp. 201-209, 31 January 1972.
- [5] H. W. Kerr and W. Kurz, "Solidification of peritectic alloys," *International Materials Reviews*, vol. 41, no. 4, pp. 129-168, 1996.
- [6] F. Devred, "Raney-type nickel catalysts, the influence of promoters in hydrogenation and fuel cell reactions: a literature review," IMPRESS project, 2004.
- [7] N. J. E. Adkins, "Intermetallic Materials Processing in Relation to Earth and Space Solidification FP6-500635-2," *Ceram Process and Materials*, 2005.
- [8] A. M. Mullis, T. D. Bigg and N. J. Adkins, "A microstructural investigation of gas atomized Raney type Al-27.5 at.% Ni catalyst precursor alloys," *Journal of Alloys and Compounds*, vol. 648, pp. 139-148, 2015.

- [9] H. Lei, Z. Song, D. Tan, X. Bao, X. Mu, B. Zong and E. Min, "Preparation of novel Raney-Ni catalysts and characterization by XRD, SEM and XPS," *Applied Catalysis A: General*, pp. 69-76, 2001.
- [10] H. Warlimont, U. Kühn and N. Mattern, "Rapidly quenched Raney catalyst precursors," *Materials Science and Engineering: A*, vol. 226–228, pp. 900-904, 1997.
- [11] A. M. Mullis, L. Farrell, R. F. Cochrane and N. J. Adkins, "Estimation of Cooling Rates During Close Coupled-Coupled Gas Atomization Using Secondary Dendrite Arm Spacing Measurement," *Metallurgical and Materials Transactions B*, vol. 44B, no. 4, pp. 992-998, 2013.
- [12] IMPRESS, *Intermetallic Processing in Relation to Earth and Space Solidification, EU Framework VI (Integrated) Project # NMP3-CT-2004-500635-2..*
- [13] D. Tourret, G. Reinhart, C.-A. Gandin, G. N. Iles, U. Dahlborg, M. Calvo-Dahlborg and C. M. Bao, "Gas atomization of Al–Ni powders: Solidification modeling and neutron diffraction analysis," *Acta Materialia*, vol. 59, pp. 6658-6669, 2011.
- [14] D. Tourret, C.-A. Gandin, T. Volkman and D. M. Herlach, "Multiple non-equilibrium phase transformations: Modeling," *Acta Materialia*, vol. 59, no. 11, p. 4665–4677, 2011.
- [15] S. R. Montgomery, "Catalysis of organic reactions," Dekker, New York, 1981.
- [16] J. M. Bonnier, J. P. Damon and J. Masson, "New approach to skeletal nickel catalysts catalytic properties of the nickel-chromium system," *Applied Catalysis*, vol. 42, no. 2, pp. 285-297, 1988.
- [17] T. Koscielski, J. M. Bonnier, J. P. Damon and J. Masson, "Catalytic hydrogenation on raney nickel catalyst modified by chromium hydroxide deposition," *Applied Catalysis*, vol. 49, no. 1, pp. 91-99, 1989.
- [18] M. Pisarek, M. Łukaszewski, P. Winiarek, P. Kedzierzawski and M. Janik-Czachor, "Influence of Cr addition to Raney Ni catalyst on hydrogenation of isophorone," *Catalysis Communications*, vol. 10, pp. 213-216, 2008.
- [19] A. C. Larson and R. B. Von Dreele, General Structure Analysis System (GSAS), Los Alamos National Laboratory, 2004.
- [20] B. H. Toby, "EXPGUI, a graphical user interface for GSAS," *Journal of Applied Crystallography*, vol. 34, pp. 210-213, 2001.
- [21] R. H. Davies, A. T. Dinsdale, J. A. Gisby, J. A. J. Robinson and S. M. Martin, "MTDATA - Thermodynamics and Phase Equilibrium Software from the National Physical Laboratory," *CALPHAD*, vol. 26, no. 2, pp. 229-271, 2002.
- [22] M. J. Cooper, "The structure of the intermetallic phase θ (Cr-Al)," *Acta Crystallographica*, vol. 13, no. 3, p. 257, 1960.
- [23] T. C. Duong, A. Talapatra, W. Son, M. Radovic and R. Arróyave, "On the stochastic phase stability of

Ti₂AlC-Cr₂AlC," *Nature Scientific Reports*, vol. 7, 07 2017.

[24] X. Z. Li, K. Sugiyama, K. Hiraga, A. Sata and A. Yamamoto, "Crystal structure of orthorhombic epsilon-Al₄Cr," *Zeitschrift fur Kristallographie*, vol. 212, pp. 628 - 633, 1997.

[25] X. Z. Li, K. Higara, K. Sugiyama and A. Yamamoto, "Structural relationship between the e-Al₄Cr and k-Al-Cr-Ni phases, in Quasicrystals: Proceedings of the 6th International Conference on Quasicrystals, 26-30 May 1997," in *World Scientific*, Tokyo, Japan, 1998.

[26] B. B. Cao and K. H. Kuo, "Crystal structure of the monoclinic -Al₁₁Cr₂," *Journal of Alloys and Compounds*, vol. 458, p. 238-247, 2008.

List of Figures

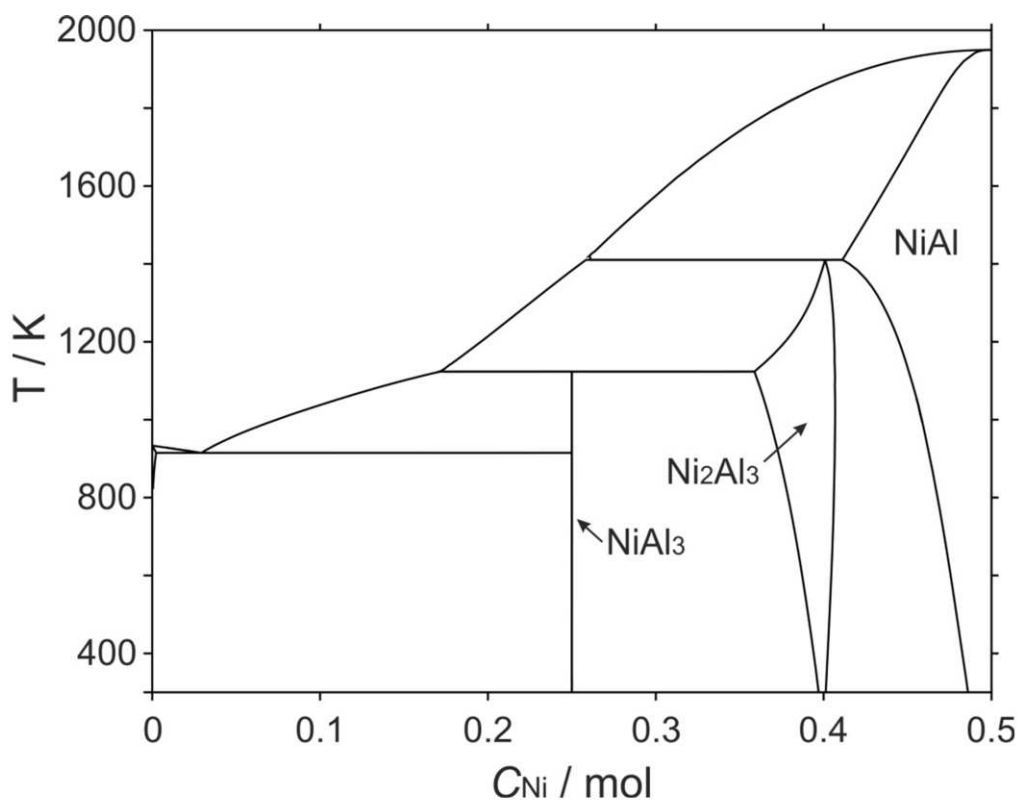


Figure 1: Al-Ni phase diagram.

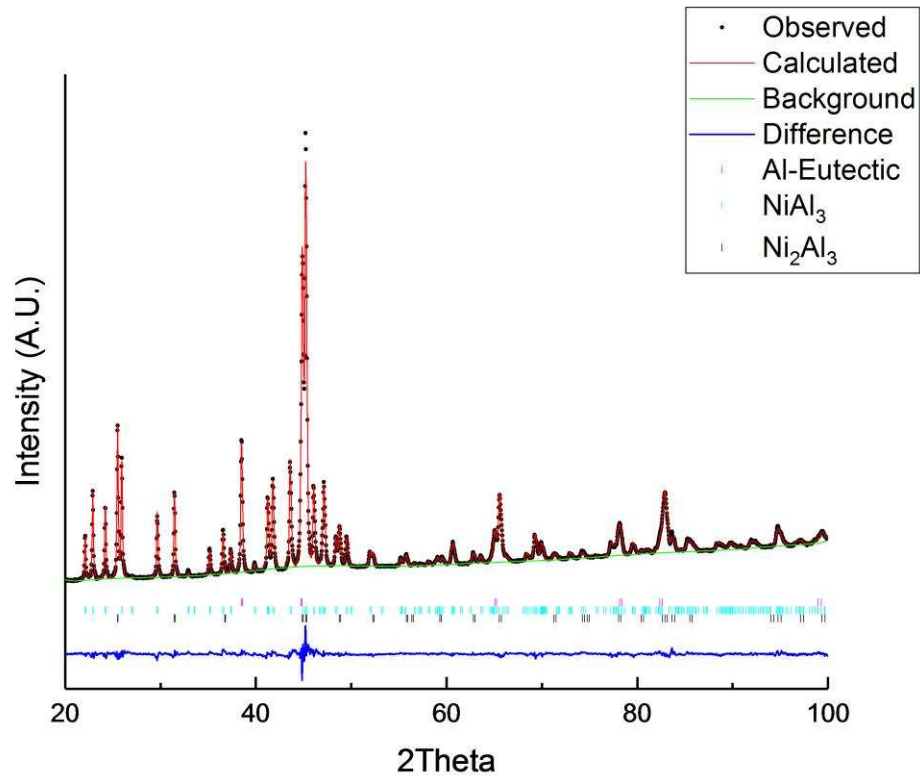


Figure 2: XRD pattern and Rietveld fit for 150μm < 212μm size fraction of Al-25 at.% Ni alloy powder.

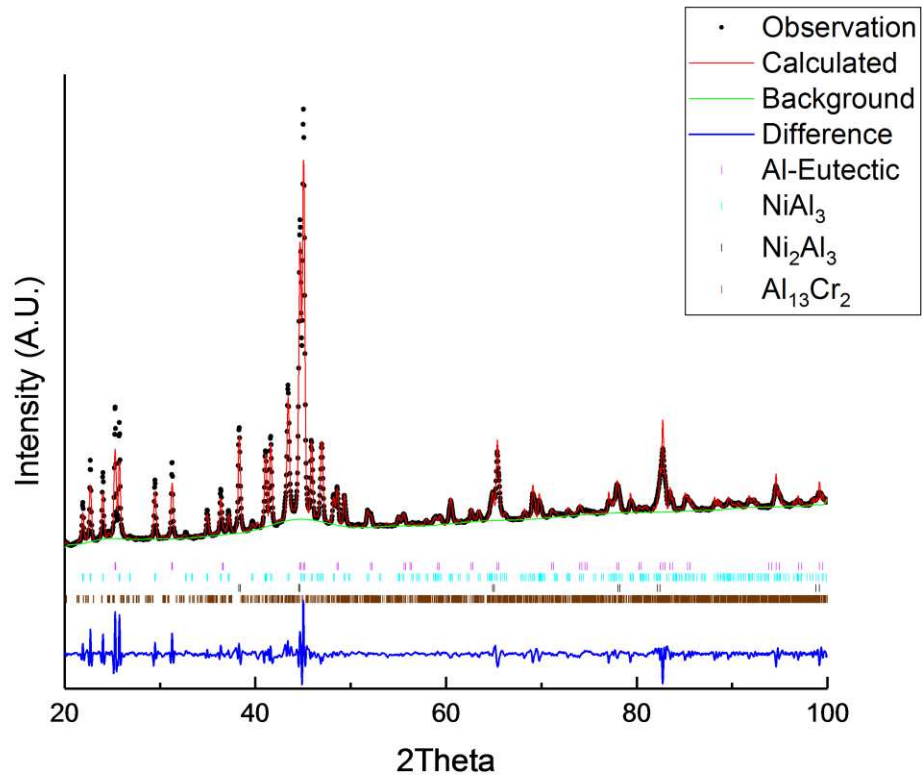


Figure 3: XRD pattern and Rietveld fit for $150\mu\text{m} < 212\mu\text{m}$ size fraction of Al-23.5 at.% Ni-1.5 at.% Cr alloy powder.

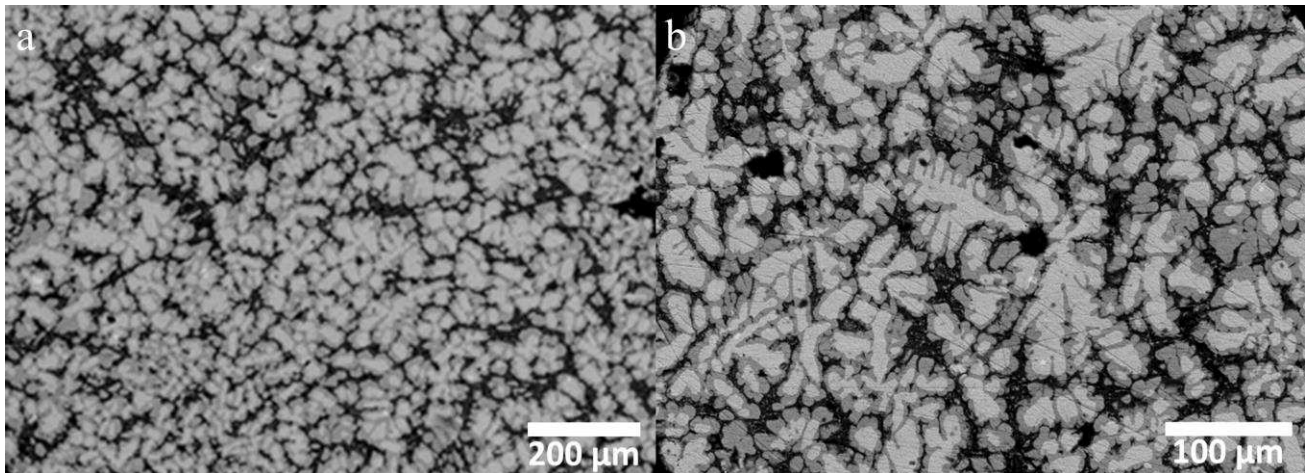


Figure 4: SEM backscatter images of Al-25 at.% Ni alloys at particle size fractions a) $150\mu\text{m} < 212\mu\text{m}$ and b) $53\mu\text{m} < 75\mu\text{m}$.

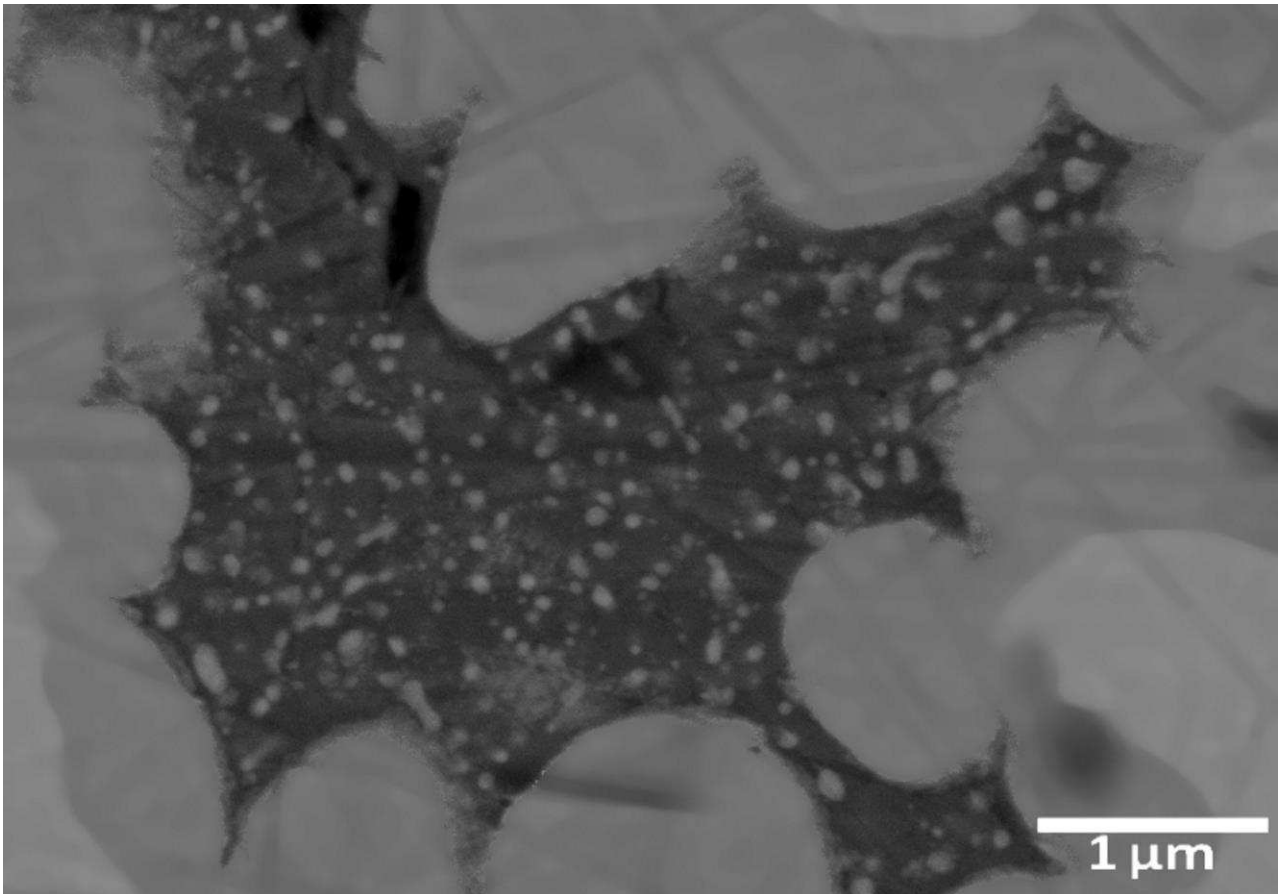


Figure 5: High magnification SEM backscatter image of $150\mu\text{m} < 212\mu\text{m}$ Al-25 at.% Ni alloy showing the Al-Al₃Ni eutectic.

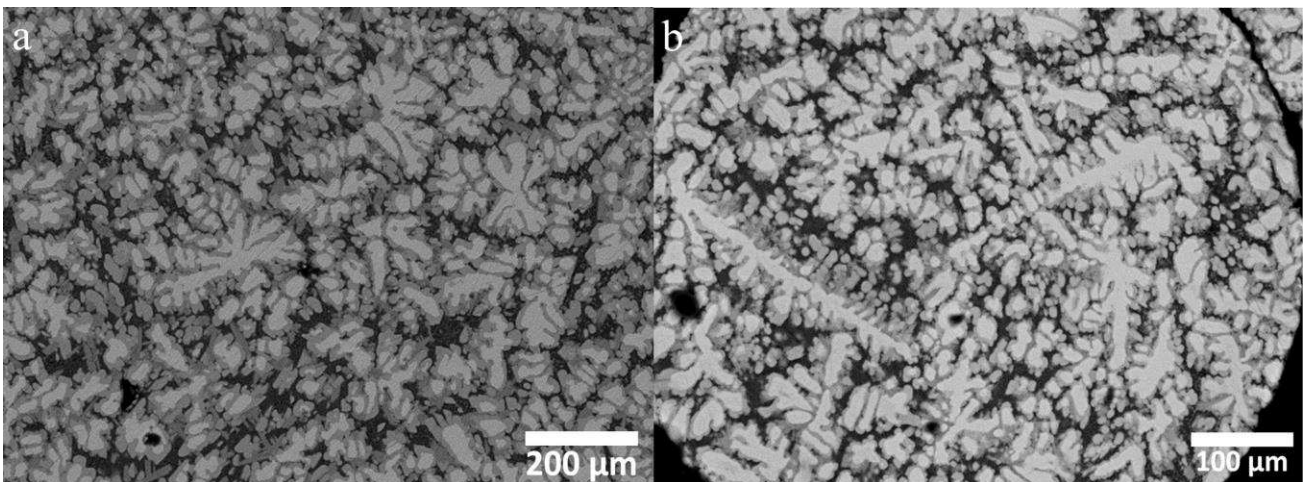


Figure 6: SEM backscatter images of Al-23.5 at.% Ni-1.5 at. % Cr alloys at particle size fractions a) $150\mu\text{m} < 212\mu\text{m}$ and b) $53\mu\text{m} < 75\mu\text{m}$.

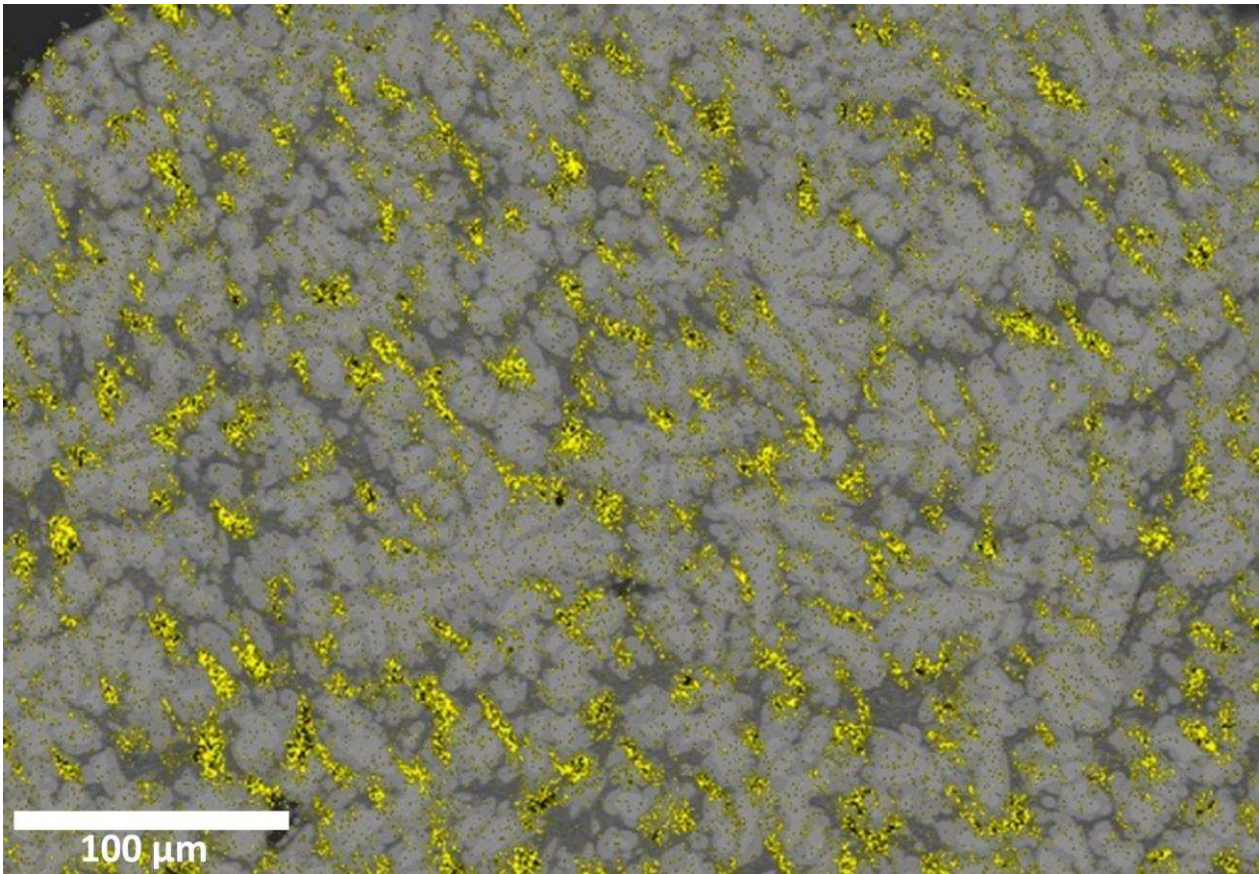


Figure 7: SEM backscatter image for $150\mu\text{m} < 212\mu\text{m}$ size fraction of the Al-23.5 at.% Ni-1.5 at.% Cr alloy overlaid with Cr EDX maps illustrating Cr localisation within the microstructure.

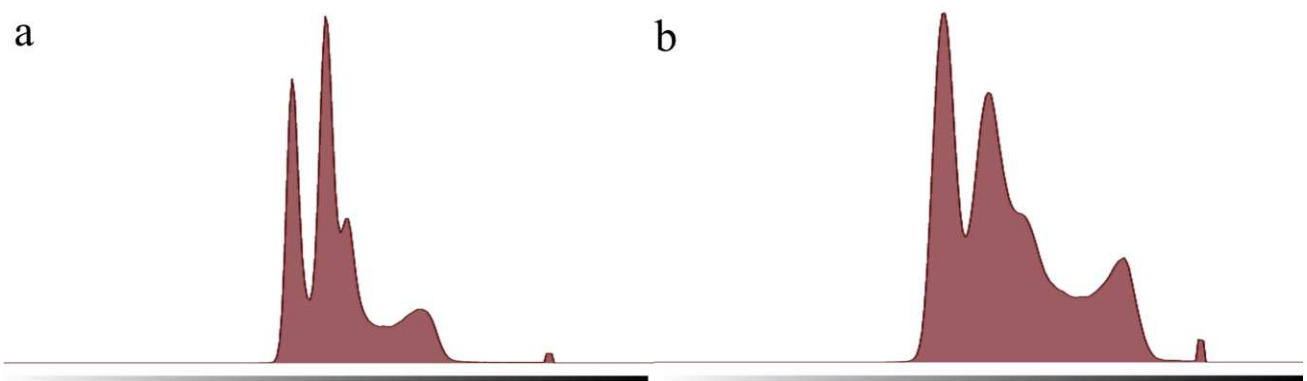


Figure 8: Colour levels of the equivalent SEM backscatter images in Figure 6 of Al-23.5 at.% Ni-1.5at%Cr alloys at particle size fractions a) $150\mu\text{m} < 212\mu\text{m}$ and b) $53\mu\text{m} < 75\mu\text{m}$.

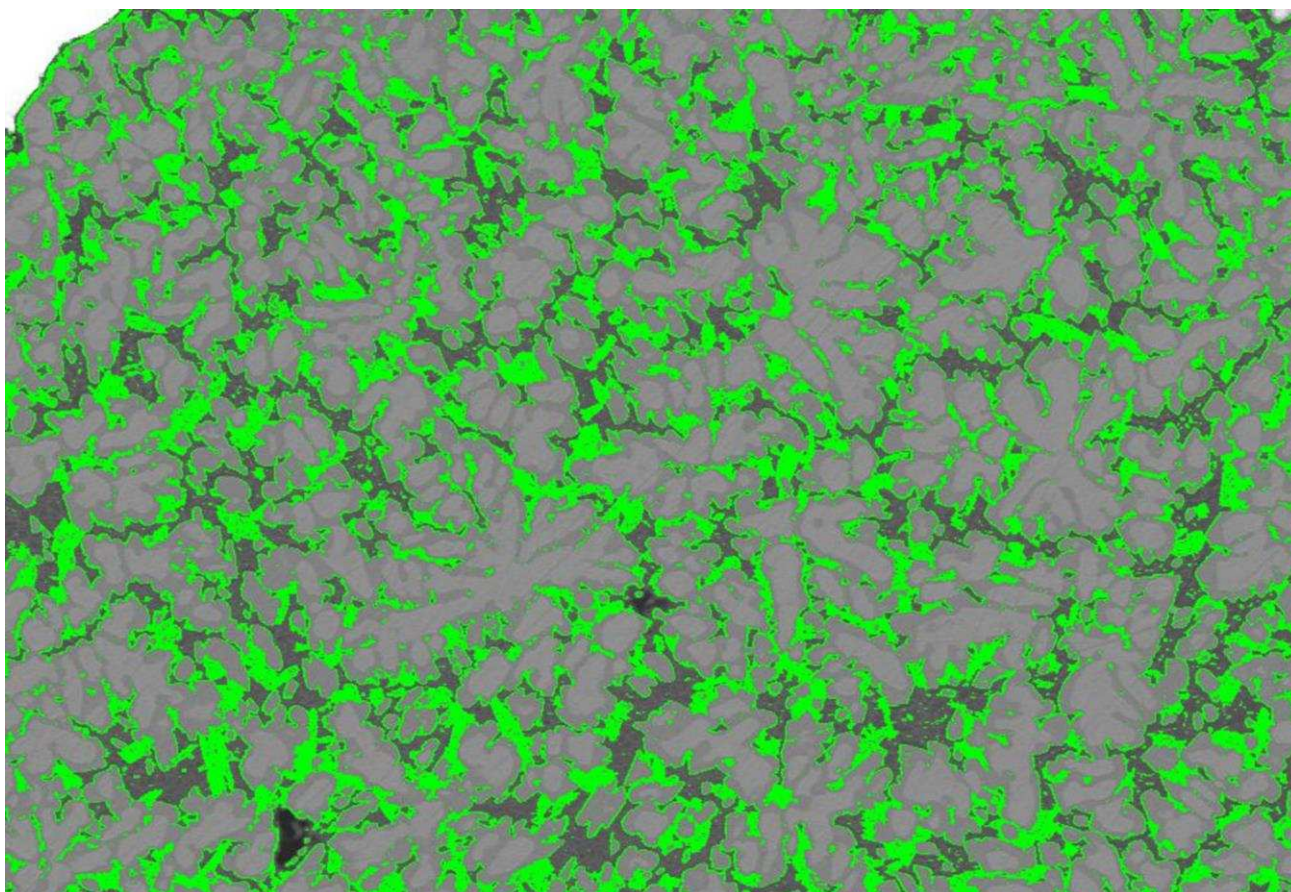


Figure 9: SEM backscatter image from Figure 7 displaying grey levels 83-101 highlighted in green.

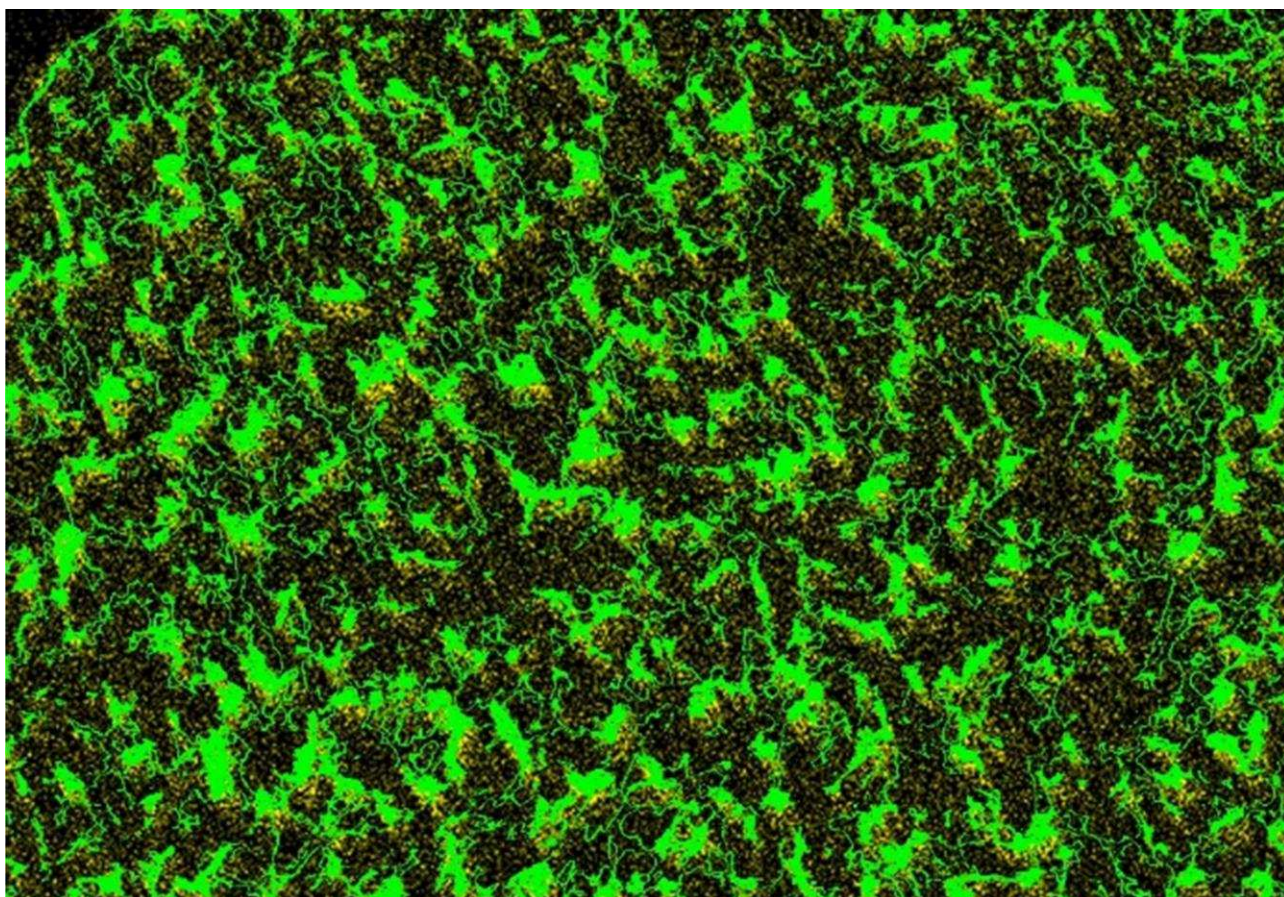


Figure 10: Cr localisation map, as given in Figure 7, obtained using EDX (yellow) overlaid with the grey level data from Figure 9 (green).